Composites Part C: Open Access 9 (2022) 100306

Contents lists available at ScienceDirect

Composites Part C: Open Access

journal homepage: www.sciencedirect.com/journal/composites-part-c-open-access

Size-effect independence of hybrid fiber-reinforced roller-compacted concrete fracture toughness

Daniela Scorza [a], Camilla Ronchei [b], Sabrina Vantadori [c,*], Andrea Zanichelli [c]

[a] Department of Engineering, University of Naples Parthenope, Naples 80143, Italy
[b] Department of Civil Engineering, University of Calabria, Arcavacata di Rende (CS) 87036, Italy
[c] Department of Engineering and Architecture, University of Parma, Parma 43124, Italy

ARTICLE INFO

Keywords:
Fracture toughness
Micromechanical numerical model
Modified Two-Parameter Model
Size-effect
Roller-compacted concrete
Three-point bending

ABSTRACT

The present paper aims to prove the size-effect independence of Hybrid Fiber-Reinforced RCC (HyFR-RCC) fracture toughness determined through the Modified Two-Parameter Model (MTPM). A micromechanical numerical model is applied to simulate the fracture behavior of seven series of single edge-notched specimens, made of both plain-RCCs and FR-RCCs (single and hybrid reinforcements), subjected to three-point bending. The MTPM is applied to the numerical load vs CMOD curves to compute the fracture toughness. A comparison with experimental values, available in the literature, is performed. Therefore, RCC specimens with different sizes are numerically simulated and the fracture toughness is analytically determined through the MTPM, proving the size-effect independence.

1. Introduction

Roller-Compacted Concrete (RCC) is a particular type of stiff-dry and zero-slump concrete, composed by dense-graded aggregates, sand, Portland cement and water, which is usually spread, with one or more bulldozers, in layers prior to compaction [1]. RCC found its first application in dams in the 1960s [2,3] becoming, in the following years, popular for the construction of pavements in storage areas, municipal and industrial roads and in rehabilitation of dams [2,4-7]. The growing interest in RCC engineering applications was principally due to both the significant costs saving and increased placement speed, with respect to the conventional Portland Cement Concrete (PCC) [4]. This is mainly due to the different proportions between the ingredients composing the RCC mixture with respect to the PCC one, with a higher percentage of fine aggregates, allowing tight packing and consolidation. Therefore, a fresh RCC stiffer than typical zero-slump concrete can be obtained. As a matter of fact, the mixture is stiff enough to remain stable under vibratory rollers and, at the same time, wet enough to permit adequate mixing and distribution of the paste without segregation [4,8,9].

Due to their common applications, RCCs are usually subjected to complex loading conditions that may cause material fatigue cracking, crack propagation and reduction of mechanical performance [10,11].

Several studies have been conducted aiming to properly design the RCC mixture proportion and to improve the material mechanical, fracture and fatigue behavior by optimising the water-to-cement ratio [12] or by using different aggregates and additives, such as Reclaimed Asphalt Pavement (RAP) [13], ceramic waste aggregates [14,15], ground calcium carbonate [16], recycled concrete aggregates [17], and industrial waste [18].

As is well known, several types of reinforcement can be used to improve the mechanical and fracture behavior of traditional concrete, such as polymeric [19], steel [20] and natural fibers [21]. Analogously, several types of reinforcing fibers, such as steel [22,23] and polymeric fibers [24,25], have been added to RCC mixture in order to obtain the same benefits observed for Fiber-Reinforced Concrete (FRC). For instance, Jia et al. [22] observed that the use of steel fibers improved the compressive strength and fracture energy of Fiber-Reinforced Roller-Compacted Concrete (FR-RCC) with respect to an ordinary FRC, whereas the fracture toughness was generally lower. Other Authors [24] investigated the fracture performance of RCC with polypropylene or steel fibers highlighting that the addition of fibers did not increase the RCC flexural strength, but significantly improved the post-peak and residual strength capacity. Instead, the fracture properties were similar or slightly greater than those of an ordinary FRC. Moreover, recent studies have demonstrated that FR-RCC has higher "fiber

* Corresponding author.
E-mail address: sabrina.vantadori@unipr.it (S. Vantadori).

https://doi.org/10.1016/j.jcomc.2022.100306
Received 29 June 2022; Accepted 8 August 2022
Available online 13 August 2022

Table 1
Material and content (% by volume) of the fibers for each of the seven mixtures examined in Ref. [31].

Mix designation	Fiber content (*% by volume*)					
	S35	S13	PP38	PM20	PP20	PP12
PC	-	-	-	-	-	-
SFRC1	-	-	-	0.7	-	-
SFRC2	0.7	-	-	-	-	-
HFRC1	0.5	-	-	-	-	0.2
HFRC2	0.5	-	-	-	0.2	-
HFRC3	-	0.2	0.5	-	-	-
HFRC4	-	0.2	-	0.5	-	-

Note: SXX: steel, PPXX: polypropylene, PMXX: polymeric material (XX stays for the fiber length in mm).

efficiency" than FRC, in terms of fiber bridging capability during crack propagation [23]. Such a behavior has been attributed to the lower water-to-cement ratio, which led to a higher friction between mortar and fibers.

Among the well-known FRCs, it is becoming common to employ more than one type of reinforcement to improve the performance of the composite materials by exploiting the beneficial interaction of the reinforcing phases [26,27]. The so-called Hybrid Fiber-Reinforced Concretes (HyFRCs) are gaining increasing popularity in several practical engineering applications, such as pavements, structural repairs and offshore constructions due to the synergic effect of various fiber combinations [28,29]. The positive interaction derived by fibers, characterized by different geometry and mechanical properties, results in more efficient fracture behavior of HyFRCs [30].

As far as the RCC is concerned, from a careful examination of the state of the art, it can be realized that only few works on Hybrid Fiber-Reinforced Roller-Compacted Concretes (HyFR-RCCs) have been published, needing further investigations [31]. Recently, Scorza et al. [31] have experimentally investigated the fracture properties of HyFR-RCC notched specimens, reinforced with several combinations of steel and polymeric fibers, subjected to three-point bending tests. In such a work, the fracture toughness has been analytically determined by means of the Modified Two-Parameter Model (MTPM) and the effect of the reinforcing fibers combinations on such a parameter has been evaluated.

The MTPM, based on the well-known Two-Parameter Model [32], was originally proposed by some of the present Authors [33] in order to correctly estimate the material fracture toughness when crack deflection (kinked crack) appears during the stable crack propagation, even in the case of far-field Mode I loading [33,34]. The above MTPM has been recently applied to different materials characterized by internal heterogeneity and for which crack deflection has been experimentally observed, such as bone [33], fiber-reinforced concrete and mortar [34-36] and particleboard (PB) [37]. Note that, the fracture toughness obtained by employing the MTPM has proved to be size-independent.

The aim of the present paper is to prove that the MTPM fracture toughness of HyFR-RCC is a size-independent parameter. In particular, specimens characterized by the seven different HyFR-RCC mixtures analysed in Ref. [31] are here considered and the fracture toughness is determined by employing a micromechanical finite element model [38-42] in conjunction with the Modified Two-Parameter Model [33,34]. More precisely, for each of the above seven HyFR-RCC specimen series: (i) the numerical model is calibrated by exploiting the experimental data reported in Ref. [31]; (ii) the load vs Crack Mouth Opening Displacement (CMOD) curves numerically obtained are used, in conjunction with the MTPM, to compute the fracture toughness; (iii) the specimen geometrical sizes are made to vary in the numerical model and the corresponding fracture toughness values are computed.

The manuscript is structured in the following Sections: in Section 2, the experimental campaign used for model calibration is briefly summarized, whereas the employed micromechanical numerical model is described in Section 3. Section 4 deals with the MTPM application to the numerical load-CMOD curves and the discussion of the results obtained in terms of fracture toughness in order to prove its size-independence. Conclusions are summarized in Section 5. It is worth noting that the description of both MTPM and micromechanical finite element model formulations are reported in **Appendices A.1** and **A.2**, respectively.

2. Experimental campaign used for the model calibration

The experimental campaign, reported in Ref. [31] and used for the model calibration, is here briefly summarized. More precisely, three-point bending tests were performed on different HyFR-RCC mixtures according to the MTPM [33] and RILEM standards [43,44].

2.1. Material and specimens

The tested specimens were made of a zero-slump cementitious paste, suitable for RCC applications, obtained by using a Portland cement type II (32.5 CEM II/B-LL) and river aggregates with a nominal maximum aggregate size of 19*mm* and a grading curve in accordance with ACI report 325.10 [4]. The matrix mixture proportions adopted for both plain and fiber-reinforced RCC were cement: water: aggregate (by weight) = 1:0.45:4.5.

For the reinforcing fibers, randomly distributed in the matrix, six types of fibers were considered, where the material and content (% by volume), for each of the HyFR-RCC mixtures examined in Ref. [31], are summarized in Table 1.

Details regarding the geometrical sizes and physical/mechanical properties of such fibers may be found in Ref. [31].

The specimens are single-edge notched beams, characterized by a prismatic shape with the following geometric sizes [31,33-35]: width $B = 50mm$, depth $W = 100mm$, length $L = 500mm$, span $S = 400mm$ and notch length $a_0 = 33.33mm$, with a notch width $< 3mm$.

For each of the above mixtures, eight specimens were prepared [31]. Such specimens were compacted on vibrating table with a surcharge of 12.7 kg, according to the ASTM C1176 standard regarding RCC pavements [45], and then cured in water for 28days. Finally, a notch was realized in the middle cross-section of each specimen.

Table 2
Mean value μ and standard deviation σ of P_{max}, $CMOD_{peak}$, E and $K^{S}_{(I+II)C}$ for each of the tested specimen series [31].

Specimen series	P_{max} [kN]		$CMOD_{peak}$ [mm]		E [GPa]		$K^{S}_{(I+II)C}$ [MPa·m$^{0.5}$]	
	μ	σ	μ	σ	μ	σ	μ	σ
PC	1.842	0.160	0.040	0.006	27.943	2.868	0.937	0.084
SFRC1	1.765	0.389	0.043	0.011	27.342	4.570	0.899	0.163
SFRC2	2.076	0.294	0.040	0.013	30.149	4.188	1.052	0.149
HFRC1	1.852	0.157	0.045	0.010	29.700	1.767	1.011	0.060
HFRC2	1.818	0.133	0.038	0.007	30.428	0.705	0.937	0.071
HFRC3	2.019	0.248	0.049	0.012	27.502	3.931	1.055	0.136
HFRC4	2.114	0.223	0.036	0.005	30.088	2.238	1.090	0.076

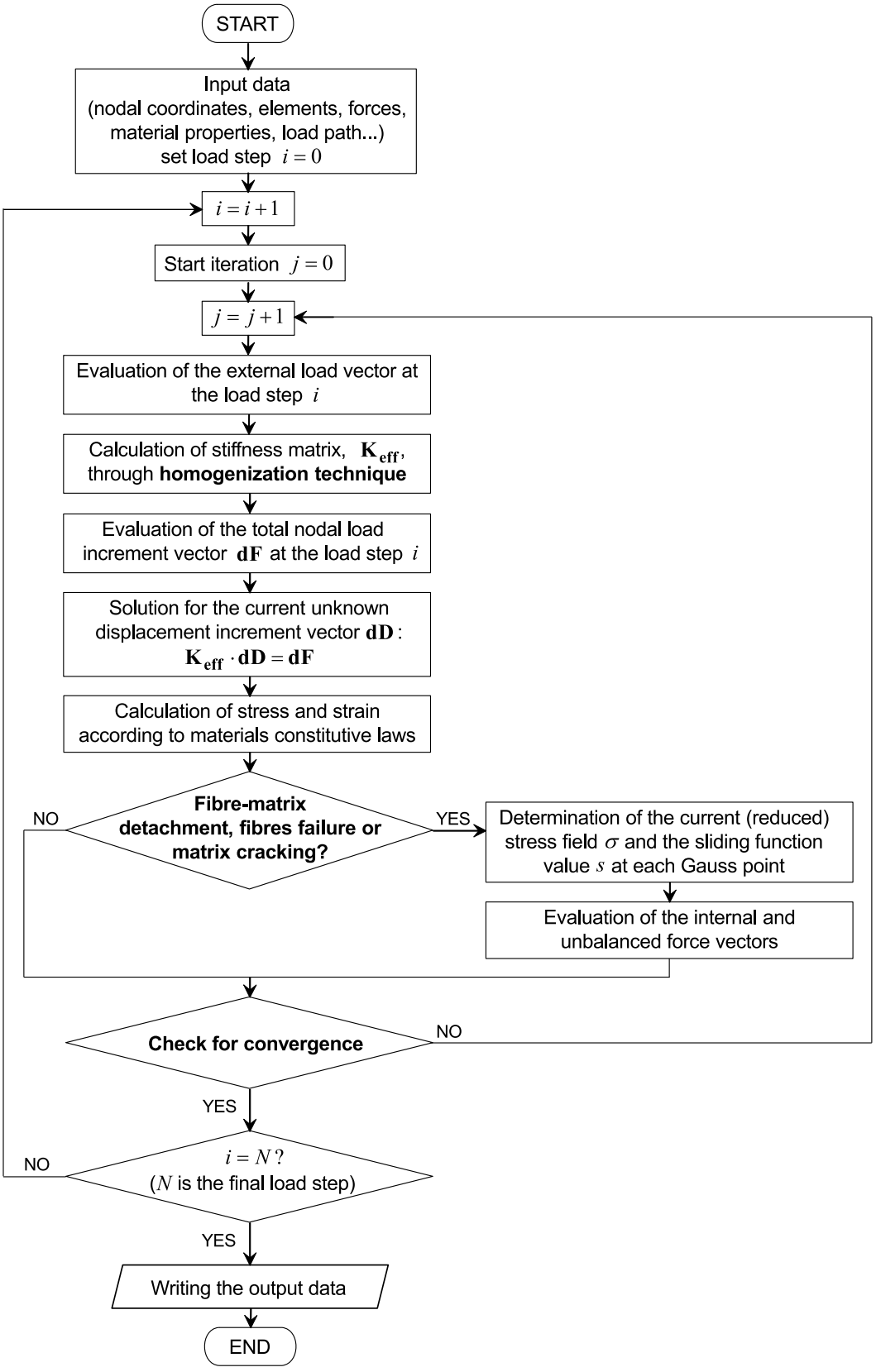

Fig. 1. Micromechanical numerical model flowchart.

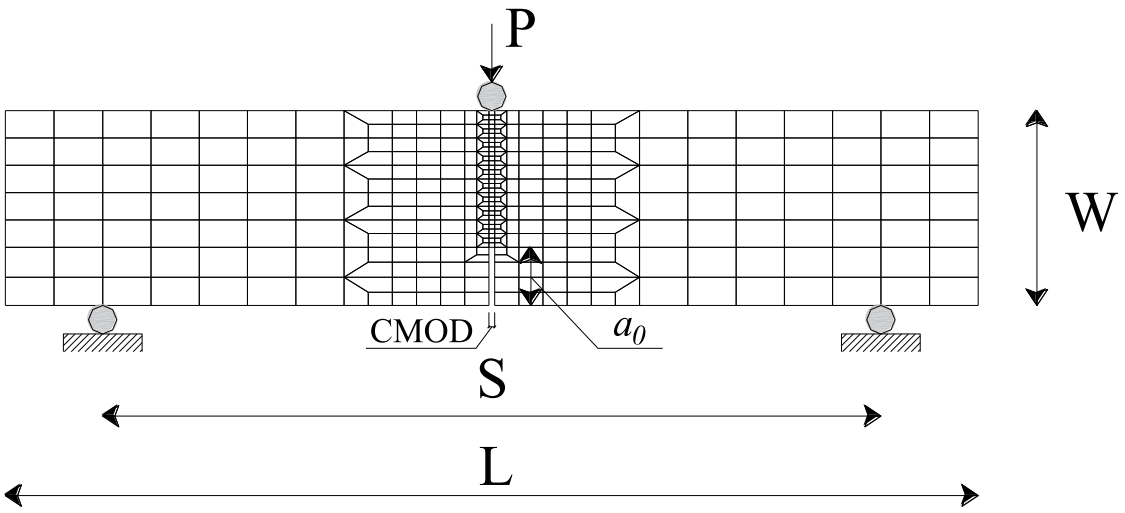

Fig. 2. 2D finite element model: sizes, loading configuration and discretization performed by means of four-node quadrilateral finite elements.

2.2. Testing conditions

The experimental campaign was carried out at the "Testing Laboratory of Materials and Structures" of the University of Parma, by means a servo-hydraulic universal testing machine Instron 8862 [31].

The specimens were subjected to three-point bending tests to evaluate the material fracture behavior. Tests were performed according to the TPM [32] and the RILEM Recommendations [43,44], that is, according to the following procedure: (i) each specimen was monotonically loaded up to the peak load, P_{max}, under Crack Mouth Opening Displacement (CMOD) control at an average rate equal to $0.1 mm h^{-1}$; (ii) at the 95% P_{max} during the post-peak stage, the specimen was fully unloaded under load control; (iii) the specimen was then reloaded up to failure under CMOD control.

2.3. Results

On the basis of the experimental results, both the elastic modulus, E, and the fracture toughness, $K^S_{(I+II)C}$ (i.e. the critical mixed mode Stress Intensity Factor, SIF), were computed according to the MTPM (see **Appendix A.1** for calculation).

The average values of peak load, P_{max}, Crack Mouth Opening Displacement at the peak load, $CMOD_{peak}$, elastic modulus, E, and fracture toughness, $K^S_{(I+II)C}$, are listed in Table 2 for each specimen series together with the corresponding standard deviations [31].

3. Micromechanical numerical model

In the present research work, a micromechanical numerical model, proposed by some of the present authors [38,41], is applied to evaluate the fracture behavior of the RCCs in terms of load vs CMOD curve.

A flowchart giving a schematic description of the micromechanical model is shown in Fig. 1.

More in details, the above micromechanical model has been implemented in a non-linear 2D Finite Element (FE) home-made code in standard Fortran language [41].

By starting from the input data, regarding the specimen geometry, the materials properties, and the boundary and loading conditions, the code framework may be summarized in the following steps:

1 the stiffness matrix, named $\mathbf{K}_{\text{eff}}$, is computed and assembled by exploiting the homogenization technique presented in Section 3.1;
2 after the definition of the nodal load increment vector, **dF**,the current displacement increment vector, **dD**, is computed;
3 the stress and strain fields are then determined according to the materials constitutive laws;
4 the stresses and strains in each finite element are then used to check if the conditions of fiber-matrix interface detachment, fiber failure and matrix cracking are reached; if so, stress and strain fields are updated as discussed in Sections 3.2 and 3.3, and the vectors of the internal and unbalanced forces are written;
5 the convergence at the current load step is checked in terms of incremental displacement norm and unbalanced forces;
6 if the required convergence conditions are satisfied, the calculation proceeds to the further load increment, by updating the stiffness matrix, otherwise, a new iteration begins from step No. 1.

The above steps are repeated until the final load increment is reached. Further details may be found in Ref. [41].

3.1. Homogenization technique

The macroscopic mechanical behavior of the composite material is obtained by adopting a homogenization technique based on the energetic formulation proposed by Kalamkarov and Liu [46].

The heterogeneous (composite) material is supposed to be composed by one matrix phase, denoted by the subscript m, and by n different fiber phases embedded in the matrix. The fundamental hypothesis is that each fiber phase is homogeneously distributed inside the matrix, implying that the composite is considered macroscopically homogeneous (see details in **Appendix A.2**). The following volume fractions of each component can be defined as:

$$\mu_m = \frac{V_m}{V} \text{ matrix volume fraction} \tag{1a}$$

$$\mu_f^p = \frac{V_f^p}{V} \text{ volume fraction of the } p-th \text{ fibre phase} \tag{1b}$$

where V_m, V_f^p and V are the matrix volume, the volume of the p-th fiber phase and the total volume, respectively.

The basic assumptions regarding the mechanical properties of the constituents are: (i) both fibers and matrix are linearly elastic, where the matrix is isotropic and the fibers have a uniaxial mechanical behavior; (ii) fibers are cylindrical and identical in shape and size; (iii) fiber and matrix interface bond is perfect (the debonding mechanism, quantified through a sliding function, is introduced in the next Sub-Section).

Under the previous hypotheses, the average properties of the composite material can be determined by equating the virtual work rate of

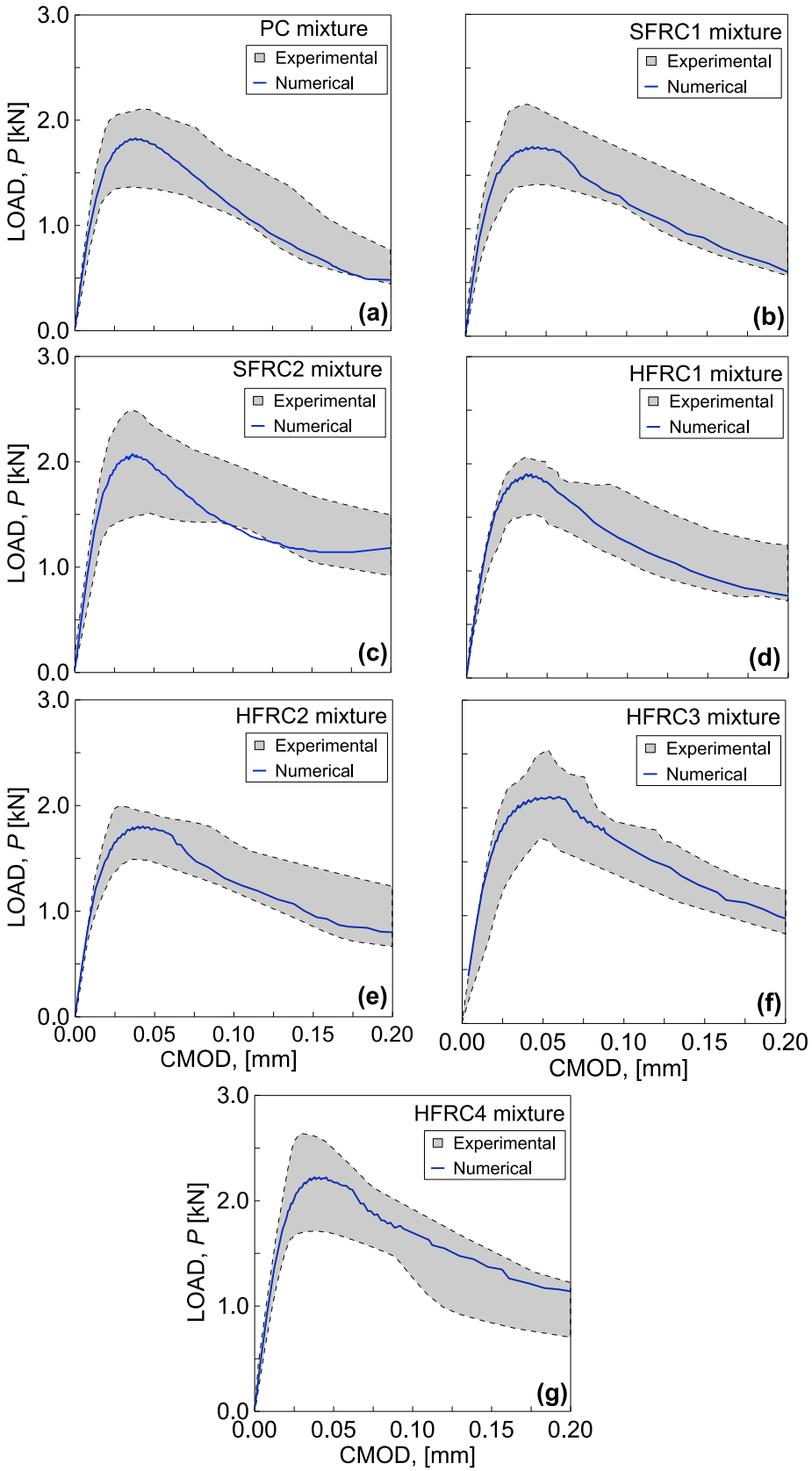

Fig. 3. Numerical load vs CMOD curves compared with experimental data [31] for specimen series: (a) PC, (b) SFRC1, (c) SFRC2, (d) HFRC1, (e) HFRC2, (f) HFRC3, (g) HFRC4.

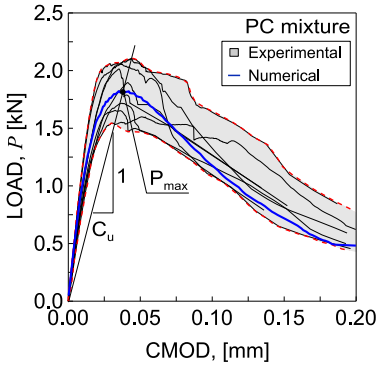

Fig. 4. Example of grey scatter band definition for the PC mixture and C_u calculation.

the composite to that of the homogenized equivalent material. The equivalent elastic tensor, $\mathbf{C}_{eq}$, of the homogenized material may be written as [41]:

$$\mathbf{C}_{eq} = \mu_m \cdot \mathbf{C}_m + \sum_{p=1}^{n} \mu_f^p \cdot \mathbf{C}_f^p \tag{2}$$

where $\mathbf{C}_m$ and $\mathbf{C}_f^p$ are the elastic tensor of the matrix and of the *p-th* fiber phase, respectively.

The spatial arrangement of the fibers is taken into account by means of a statistical function, describing their orientation, and implemented in $\mathbf{C}_f^p$ matrix. Details may be found in **Appendix A.2** and Refs [39,41].

3.2. Fiber-matrix debonding modelling

Fiber-reinforced materials suffer from loss of fiber-matrix bond effectiveness, with a consequent detrimental effect on the stress transferred between the different constituents. Such a phenomenon, known as debonding, is one of the most common damage mechanisms in fiber-reinforced composites and it is represented by a partial or complete detachment between the phases of the composite. The debonding is due to the local stress concentration at fiber-matrix interface, caused by both their different elastic properties and the geometric discontinuities introduced by the fibers embedded in the matrix.

Eq. (2), presented in the Section 3.1, is written under the hypothesis of a perfect bond between the fibers and the matrix, so that the fiber strain, ε_f, is equal to the matrix strain along the fiber direction, ε_m^f. However, when an imperfect bond between fiber and matrix takes place, a strain jump, named $\varepsilon_{m-f}(\mathbf{x})$, is assumed at the fiber-matrix interface.

Table 3
Experimental and numerical values of P_{max}, $CMOD_{peak}$, E and $K^S_{(I+II)C}$ for each specimen series, together with the percentage error.

Specimen series	P_{max} [kN]			$CMOD_{peak}$ [mm]			E [GPa]			$K^S_{(I+II)C}$ [MPa·m$^{0.5}$]		
	EXP	NUM	err[%]	EXP	NUM	err[%]	EXP	NUM	err[%]	EXP	NUM	err[%]
PC	1.842	1.826	-1.0	0.040	0.037	-8.2	27.943	27.299	-2.3	0.937	0.967	3.2
SFRC1	1.765	1.727	-2.2	0.043	0.039	-9.1	27.342	27.540	0.7	0.899	0.941	4.7
SFRC2	2.076	2070	-0.3	0.040	0.036	-8.5	30.149	30.798	2.2	1.052	1.108	5.3
HFRC1	1.852	1.900	2.6	0.045	0.041	-8.2	29.700	29.956	0.9	1.011	1.083	5.6
HFRC2	1.818	1.800	-1.0	0.038	0.039	2.6	30.428	30.559	0.4	0.937	0.966	3.1
HFRC3	2.019	2.058	1.9	0.049	0.049	0.4	27.502	28.012	1.9	1.055	1.128	**6.9**
HFRC4	2.114	2.176	**2.9**	0.036	0.038	5.0	30.088	30.858	**2.6**	1.090	1.147	5.2

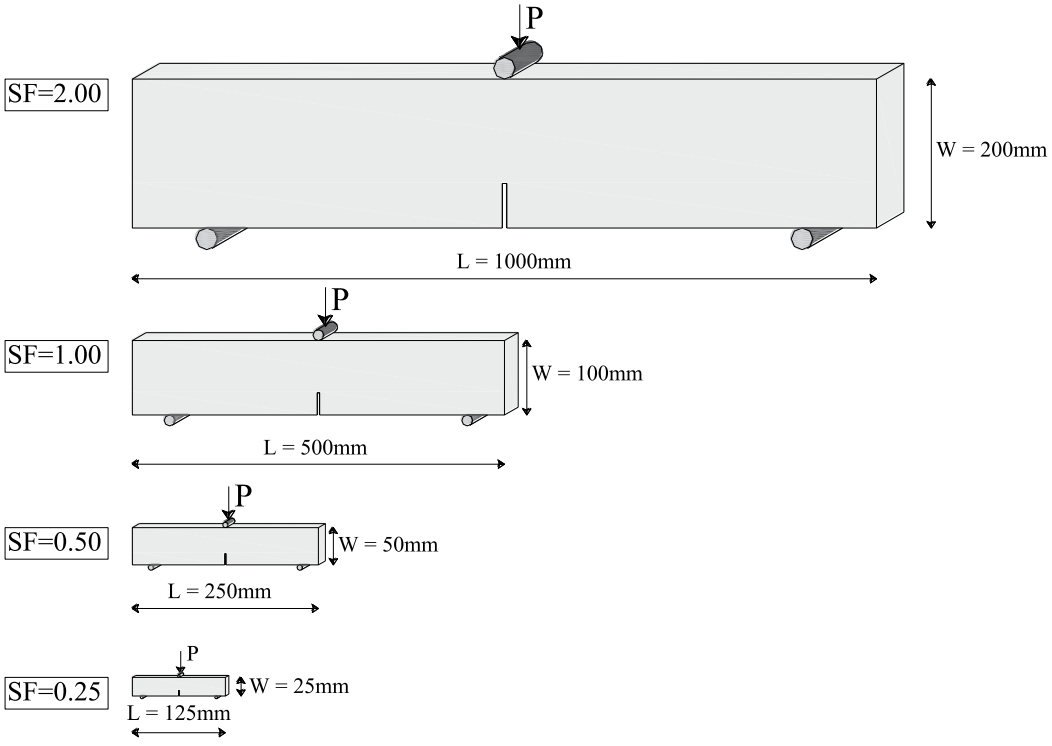

Fig. 5. The four different models considered in terms of geometrical sizes.

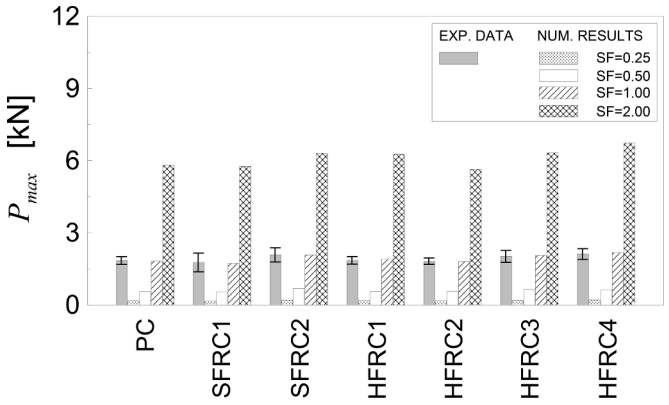

Fig. 6. Experimental and numerical values (related to the four values of the scale factor, *SF*) of the peak load, P_{max}, for each specimen series. Also the standard deviation error bars are represented for the experimental results.

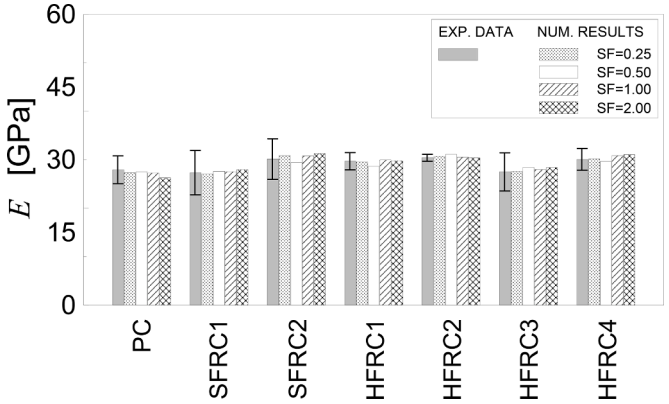

Fig. 7. Experimental and numerical values (related to the four values of the scale factor, *SF*) of the elastic modulus, *E*, for each specimen series. Also the standard deviation error bars are represented for the experimental results.

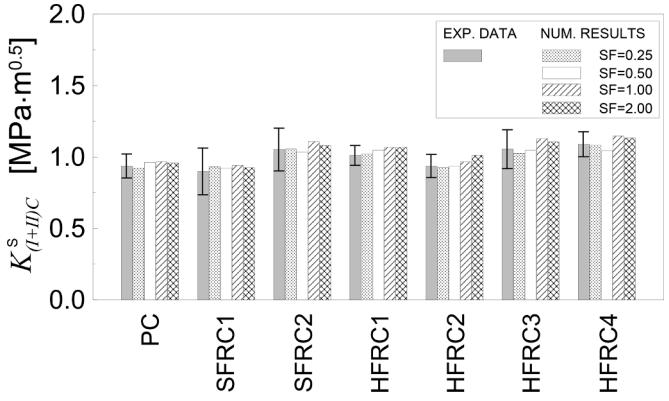

Fig. 8. Experimental and numerical values (related to the four values of the scale factor, *SF*) of the fracture toughness, $K^{S}_{(I+II)C}$, for each specimen series. Also the standard deviation error bars are represented for the experimental results.

Such a strain jump at a generic spatial point, identified by the vector **x**, can be written as [41]:

$$\varepsilon_{m-f}(\mathbf{x}) = \varepsilon^{f}_{m}(\mathbf{x}) - \varepsilon_{f}(\mathbf{x}) \tag{3}$$

where $\varepsilon^{f}_{m}(\mathbf{x})$ and $\varepsilon_{f}(\mathbf{x})$ are the matrix strain along the fiber direction and the fiber strain, respectively. In order to write a relationship depending only on the matrix strain, a sliding function, $s(\varepsilon^{f}_{m}(\mathbf{x}))$, is introduced and the strain jump is rewritten as:

$$\varepsilon_{m-f}(\mathbf{x}) = \varepsilon^{f}_{m}(\mathbf{x})\left[1 - s\left(\varepsilon^{f}_{m}(\mathbf{x})\right)\right] \tag{4}$$

According to Eq. (4), the sliding function varies along the fiber length, being a function of the vector **x**. However, since the fibers are short, it is more convenient to introduce a scalar sliding function, that is, the mean value of the sliding function $s(\varepsilon^{f}_{m}(\mathbf{x}))$ along the fiber axis, $s(\overline{\varepsilon^{f}_{m}})$. Consequently, Eq. (4) becomes:

$$\varepsilon_{m-f}(\mathbf{x}) = \varepsilon^{f}_{m}(\mathbf{x})\left[1 - s\left(\overline{\varepsilon^{f}_{m}}\right)\right] \tag{5}$$

Such a scalar sliding function is then defined by means of an energy balance of the strain energy of the fiber, evaluated through the effective shear stress transmitted by the matrix [41].

The present model assumes that the debonding progressively takes place from the ends of the fiber, up to its midpoint, according to the classical "Shear Lag Model" proposed by Cox [47]. The scalar sliding function, indeed, measures the average "degree of sliding" between the fiber and the matrix. More precisely, when $s(\overline{\varepsilon^{f}_{m}})$ is equal to zero, the detachment is complete and $\varepsilon_{m-f}(\mathbf{x}) = \varepsilon^{f}_{m}(\mathbf{x})$; consequently, no shear stress is transferred between matrix and fiber. In such a case, the fiber-matrix interface has no stiffness and the fiber does not bear any stress, that is to say, the composite material behaves as an elastic material with inclusion of voids having the shape of the fibers. On the other hand, when $s(\overline{\varepsilon^{f}_{m}})$ is equal to 1, the fiber-matrix bond is perfect, i.e. no strain jump occurs and $\varepsilon_{m-f}(\mathbf{x}) = 0$. In such a condition the shear stress transferred between matrix and fiber is maximum, and the reinforcing phase carries the maximum possible load.

The above scalar sliding function is included in the elastic tensor of the *p-th* fiber phase, $\mathbf{C}^{p}_{f}$. Details may be found in **Appendix A.2** and Refs [41,48].

3.3. Fracture behavior modelling

In the present micromechanical model, the matrix is assumed to have a brittle behavior and the discontinuities due to the fracture process are modelled through a suitable modification of the material properties. In particular, since the above model is implemented in a Finite Element code, the nucleation of one or more cracks in the finite elements is related to the reduction of the current matrix stiffness in correspondence of the integration points.

In order to describe the matrix fracture process, a cohesive-friction law is introduced to simulate the cracked zone, whereas an elastic law is adopted for the non-cracked (continuous) region. In particular, the crack faces are assumed to transmit a non-zero stress, which depends on a continuous decreasing exponential law of the relative crack opening displacement, based on the formulation proposed by Sancho et al. [49].

On the other hand, the fibers are assumed to behave elastically, and their possible failure is taken into account when the maximum tensile stress along the fiber axis reaches the material tensile strength.

To interested readers, details may be found in Refs [38,41].

4. Results and discussion

In this Section, the micromechanical model described in Section 3 is applied to simulate the experimental campaign described in Section 2, in order to calibrate the model. More precisely, firstly the numerical load vs CMOD curves are obtained for each specimen series of the experimental campaign; then, the fracture toughness is computed by means of the MTPM. After the model calibration, the specimen geometrical sizes are made to vary in the numerical model and the fracture toughness is computed by following the above procedure.

Table 4
Experimental and numerical values (related to the four values of the scale factor, *SF*) of P_{max} for each specimen series. The ratio between numerical and experimental values, $R = P_{max}^{(num)}/P_{max}^{(exp)}$, is also reported.

Specimen series	P_{max} [kN]								
	EXP	$SF = 0.25$		$SF = 0.50$		$SF = 1.00$		$SF = 2.00$	
		NUM	R [-]	NUM	R [-]	NUM	R [-]	NUM	R [-]
PC	1.842	0.176	0.1	0.550	0.3	1.826	1.0	5.803	3.2
SFRC1	1.765	0.161	0.1	0.544	0.3	1.727	1.0	5.762	3.3
SFRC2	2.076	0.193	0.1	0.690	0.3	2070	1.0	6.300	3.0
HFRC1	1.852	0.178	0.1	0.550	0.3	1.900	1.0	6.268	3.4
HFRC2	1.818	0.173	0.1	0.560	0.3	1.800	1.0	5.634	3.1
HFRC3	2.019	0.185	0.1	0.643	0.3	2.058	1.0	6.317	3.1
HFRC4	2.114	0.202	0.1	0.618	0.3	2.176	1.0	6.732	3.2

Table 5
Experimental and numerical values (related to the four values of the scale factor, *SF*) of *E* for each specimen series. The percentage error is also reported.

Specimen series	*E* [GPa]								
	EXP	$SF = 0.25$		$SF = 0.50$		$SF = 1.00$		$SF = 2.00$	
		NUM	err [%]	NUM	err [%]	NUM	err [%]	NUM	err [%]
PC	27.943	27.351	-2.1	27.501	-1.6	27.299	-2.3	26.294	**-5.9**
SFRC1	27.342	27.048	-1.1	27.632	1.1	27.540	0.7	27.974	2.3
SFRC2	30.149	30.860	2.4	29.466	-2.3	30.798	2.2	31.289	3.8
HFRC1	29.700	29.580	-0.4	28.630	-3.6	29.956	0.9	29.799	-0.3
HFRC2	30.428	30.726	1.0	31.121	2.3	30.559	0.4	30.391	0.1
HFRC3	27.502	27.583	0.3	28.430	3.4	28.012	1.9	28.388	3.2
HFRC4	30.088	30.186	0.3	29.667	-1.4	30.858	2.6	31.052	3.2

Table 6
Experimental and numerical values (related to the four values of the scale factor, *SF*) of $K^S_{(I+II)C}$ for each specimen series. The percentage error is also reported.

Specimen series	$K^S_{(I+II)C}$ [MPa·m$^{0.5}$]								
	EXP	$SF = 0.25$		$SF = 0.50$		$SF = 1.00$		$SF = 2.00$	
		NUM	err [%]	NUM	err [%]	NUM	err [%]	NUM	err [%]
PC	0.937	0.920	-1.8	0.962	2.7	0.967	3.2	0.958	2.2
SFRC1	0.899	0.931	3.6	0.921	2.4	0.941	4.7	0.925	2.9
SFRC2	1.052	1.056	0.3	1.034	-1.7	1.108	5.3	1.080	2.6
HFRC1	1.011	1.021	1.0	1.048	3.7	1.068	5.6	1.067	5.5
HFRC2	0.937	0.927	-1.1	0.938	0.1	0.966	3.1	1.012	**8.0**
HFRC3	1.055	1.026	-2.8	1.047	-0.8	1.128	6.9	1.107	4.9
HFRC4	1.090	1.082	-0.7	1.044	-4.2	1.147	5.2	1.132	3.9

4.1. Micromechanical model calibration

The prismatic specimens subjected to three-point bending loading are modelled with the nominal sizes reported in **Section 2.1**, by using a mesh discretization composed of 366 four-node plate elements and by assuming a plane stress condition (as shown in **Fig. 2**). The presence of the notch, with a thickness equal to 3 mm is also modelled.

According to the experimental evidences, the mechanical properties of the matrix material are assumed as follows: Young modulus E_m equal to $27.94GPa$, Poisson's ratio ν_m equal to 0.2, ultimate tensile strength f_t equal to $3.96MPa$, and energy release rate G_f equal to $40N/m$; whereas the mechanical properties of the fiber phases are reported in Ref. **[31]**. The fibers are supposed to be randomly oriented and homogeneously distributed into the matrix.

The analyses are performed under displacement control, by imposing a progressive vertical displacement at the top central loaded point and measuring the corresponding reaction force. The vertical load against the CMOD curves for the examined seven specimen series are compared with the experimental ones in **Fig. 3**.

More precisely, for each series, such a numerical curve (represented by the continuous thick line) is plotted together with the corresponding experimental scatter band (represented by the grey area between the two discontinuous thin lines). Such experimental scatter bands are obtained according to the following procedure: firstly, all the experimental curves related to the same specimen series are plotted; then, the external contour is retraced by the discontinuous thin lines in red; the experimental scatter band is the region inside the red lines and it is highlighted in grey. An example of the above procedure is shown in **Fig. 4** for the PC mixture.

From **Fig. 3**, it can be observed that the experimental scatter bands are predicted in a quite-satisfactory way by the numerical curves and a good correspondence can be highlighted for each specimen series in the initial elastic stage, at the peak-load and in the post-peak softening branch.

The elastic modulus and the fracture toughness are computed by means of the Modified Two-Parameter Model, applied to the above numerical curves. In particular, in **Table 3**, both the average experimental data and the corresponding numerical results are listed for each examined specimen series in terms of peak load, P_{max}, crack mouth opening displacement at the peak load, $CMOD_{peak}$, elastic modulus, E, and fracture toughness, $K^S_{(I+II)C}$, together with the error in percentage.

Since in the numerical analyses the unloading and reloading branches of the experimental tests are not simulated, the unloading compliance, C_u, is estimated at the peak load instead of employing the unloading branch slope, as shown in **Fig. 4**.

From **Table 3**, it can be observed that all the experimental values are well-predicted by the numerical approach (that is, the micromechanical numerical model in conjunction with the MTPM) being the errors lower than 10% for all the cases. In particular, the maximum error related to:

(i) the peak load estimation is equal to about 2.9% for the HFRC4 mixture; (ii) the elastic modulus estimation is equal to about 2.6% for the HFRC4 mixture; and (iii) the fracture toughness estimation is equal to about 6.9% for the HFRC3 mixture.

4.2. Analysis of the size-effect on fracture behavior

As previously observed, the numerical results are in good agreement with the experimental data, showing that the micromechanical model is able to properly estimate the material fracture toughness. Therefore, such a model is employed in the following to prove the size-effect independence of RCC fracture toughness determined by applying the model in conjunction with the MTPM.

Within this purpose, four different models in terms of geometrical sizes are considered. More precisely, each size of the tested specimen is multiplied by a scale factor (named in the following *SF*), and four *SFs* are considered (Fig. 5): 0.25, 0.50, 1.00 and 2.00. Note that, the case with $SF = 1.00$ corresponds to the tested specimen sizes simulated in Section 4.1.

The results obtained from the present models in terms of peak load, P_{max}, elastic modulus, E, and fracture toughness, $K^S_{(I+II)C}$, are plotted in Figs. 6, 7 and 8 and listed in Tables 4, 5 and 6, respectively, by considering the four scale factors for each specimen series.

By focusing the attention on the peak load (Fig. 6 and Table 4), and by taking the experimental value (represented by the bars in grey in Fig. 6) as reference, for all the specimens series it can be remarked that: (i) the computed peak load values are in good agreement with the experimental ones for the case with $SF = 1.00$; (ii) the computed peak load values are about 3 times the reference ones for the case with $SF = 2.00$; (iii) the computed peak load values are about 30% and 10% of the experimental ones for $SF = 0.50$ and $SF = 0.25$, respectively.

As far as the elastic modulus and the fracture toughness are concerned, the values estimated at different scales are almost equal to the corresponding experimental averaged values and, more precisely, are inside the experimental standard deviation error bars, for each specimen series (see Figs. 7 and 8, respectively). As a matter of fact, from Table 5 it can be observed that, by taking the averaged experimental elastic moduli as reference values, the maximum error computed is equal to 5.9% (absolute value) for the PC series with $SF = 2.00$, whereas from Table 6 it can be observed that, by taking the averaged experimental fracture toughness values as reference ones, the maximum error computed is equal to 8.0% for the HFRC2 series with $SF = 2.00$.

Therefore, the difference between the values of both elastic modulus and fracture toughness obtained for different scale factors can be considered as the result of numerical approximations. Consequently, the fracture toughness computed by exploiting the micromechanical model in conjunction with the MTPM has been proved to be size-independent.

5. Conclusions

In the present work, a micromechanical numerical model has been applied to simulate the fracture behavior of single edge-notched specimens, made of both plain RCC (without fibers) and fiber-reinforced RCCs (single and hybrid reinforcements), subjected to three-point bending tests.

Seven specimen series, characterized by different fibers contents and materials, have been considered and the obtained numerical load vs CMOD curves have been used to compute the material elastic modulus and the fracture toughness by applying the Modified Two-Parameter Model. The obtained results have been compared with experimental data available in the literature.

It has been observed that all the experimental values are well-predicted being the errors lower than 10% for all the cases and, more precisely, the maximum error is equal to about 2.9% (HFRC4 specimen series) for the peak load, 2.6% (HFRC4 specimen series) for the elastic modulus and 6.9% (HFRC3 specimen series) for the fracture toughness.

Finally, four different models, in terms of geometrical sizes, have been considered for the seven specimen series and from the numerical load vs CMOD curves the corresponding values of elastic modulus and fracture toughness have been analytically determined by means of the MTPM. It has been observed that both elastic modulus and fracture toughness estimated values are almost equal to the corresponding experimental averaged values independent of the specimen sizes, being such values inside the experimental standard deviation error bars, for all the specimen series.

According to the above satisfactory results, the fracture toughness obtained by applying the micromechanical model in conjunction with the MTPM is a size-independent parameter, that is, it depends only on the material. In conclusion, the micromechanical numerical model here employed has proved to be a useful tool to estimate the fracture parameters of fiber-reinforced cementitious-based composites.

Declaration of Competing Interest

The authors declare that they have no known competing financial interests or personal relationships that could have appeared to influence the work reported in this paper.

Acknowledgments

The work of Sabrina Vantadori and Andrea Zanichelli is supported by Italian Ministry of University and Research (P.R.I.N. National Grant 2017, Project code 2017HFPKZY; University of Parma Research Unit).

Appendix

A. The MTPM formulation

According to the original formulation of the TPM for plain concrete [32], the elastic modulus, E, is given by:

$$E = \frac{6 S\, a_0\, V(\alpha_0)}{C_i\, W^2\, B} \tag{A.1}$$

being $V(\alpha_0)$:

$$V(\alpha_0) = 0.76 - 2.28\alpha_0 + 3.87\alpha_0^2 - 2.04\alpha_0^3 + \frac{0.66}{(1-\alpha_0)^2} \tag{A.2}$$

where S is the loading span, W and B are depth and width of the specimen, respectively, a_0 is the notch length, C_i is the initial compliance (Fig. A.1) and $\alpha_0 = a_0 / W$ is the notch depth ratio.

Therefore, if the crack propagates under pure Mode I, the effective critical crack length $\underline{a}$, shown in Fig. A.2, is used to determine the critical stress-intensity factor, K_{IC}^{S}, obtained from the following equation by employing an iterative procedure:

$$E = \frac{6\,S\,\underline{a}\,V(\alpha)}{C_u\,W^2\,B} \tag{A.3}$$

where C_u is the unloading compliance (Fig. A.1), and $V(\alpha)$ is deduced from Eq.(A.2) by replacing a_0 with $\underline{a}$.

The *critical stress-intensity factor under pure Mode I*, K_{IC}^{S}, is computed as:

$$K_{IC}^{S} = \frac{3\,P_{\max}\,S}{2\,W^2\,B}\sqrt{\pi\,\underline{a}}\,f(\alpha) \tag{A.4}$$

being:

$$f(\alpha) = \frac{1}{\sqrt{\pi}}\frac{1.99 - \alpha(1-\alpha)(2.15 - 3.93\alpha + 2.70\alpha^2)}{(1+2\alpha)(1-\alpha)^{3/2}} \tag{A.5}$$

Under *Mixed mode loading*, that is according to the MTPM **[33]**, the elastic modulus, E, is given by:

$$E = \frac{6\,S}{C_u\,W^2\,B}\left\{a_0\,V\left(\frac{a_0}{W}\right) + \left[\cos^6\frac{\theta}{2} + \sin^2\frac{\theta}{2}\cos^4\frac{\theta}{2}\right]\left[(a_0 + a_1\cos\theta)\,V\left(\frac{a_0 + a_1\cos\theta}{W}\right) - a_0\,V\left(\frac{a_0}{W}\right)\right] + \right.$$
$$\left. + \left[\cos^3\theta + \sin^2\theta\cos\theta\right]\left[(a_0 + a_1\cos\theta + a_2\cos\theta)V\left(\frac{a_0 + a_1\cos\theta + a_2\cos\theta}{W}\right) - (a_0 + a_1\cos\theta)V\left(\frac{a_0 + a_1\cos\theta}{W}\right)\right]\right\} \tag{A.6}$$

where the effective critical crack length, $\underline{a} = a_0 + (a_1 + a_2)\cos\theta$ (Fig. A.3), is obtained from Eq.(A.6) through an iterative procedure, being C_u the unloading compliance (Fig. A.1), $a_1 = 0.3a_0$ and a_2 a segment of the kinked crack, and θ the crack kinking angle.

Note that, if the value of a_2 obtained from Eq.(A.6) is negative, it means that the effective crack length is $\underline{a} = a_0 + a_1\cos\theta$ with $a_1 < 0.3\quad a_0$. In this case, the length a_1 is obtained from the following equation through an iterative procedure:

$$E = \frac{6\,S}{C_u\,W^2\,B}\left\{a_0\,V\left(\frac{a_0}{W}\right) + \left[\cos^6\frac{\theta}{2} + \sin^2\frac{\theta}{2}\cos^4\frac{\theta}{2}\right]\left[(a_0 + a_1\cos\theta)\,V\left(\frac{a_0 + a_1\cos\theta}{W}\right) - a_0\,V\left(\frac{a_0}{W}\right)\right]\right\} \tag{A.7}$$

The *critical stress-intensity factor under Mixed Mode loading*, $K_{(I+II)C}^{S}$, is computed as:

$$K_{(I+II)C}^{S} = \frac{3P_{\max}S}{2W^2B}\sqrt{\pi[a_0 + (a_1 + a_2)\cos\theta]}f(\alpha) \quad with \quad \alpha = \frac{a_0 + (a_1 + a_2)\cos\theta}{W} \tag{A.8}$$

when $a_1 = 0.3\quad a_0$, whereas as:

$$K_{(I+II)C}^{S} = \frac{3P_{\max}S}{2W^2B}\sqrt{\pi[a_0 + a_1\cos\theta]}f(\alpha) \quad with \quad \alpha = \frac{a_0 + a_1\cos\theta}{W} \tag{A.9}$$

when $a_1 < 0.3\quad a_0$.

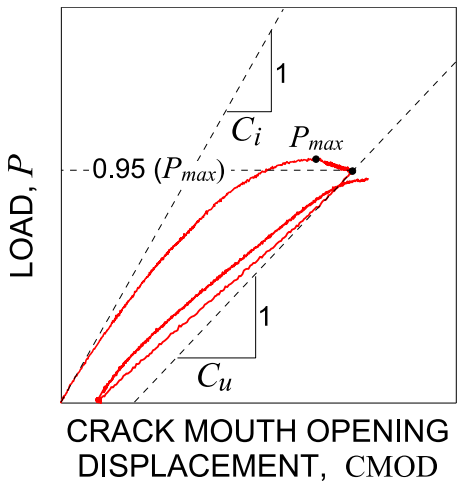

Fig. A.1. Typical load—CMOD plot.

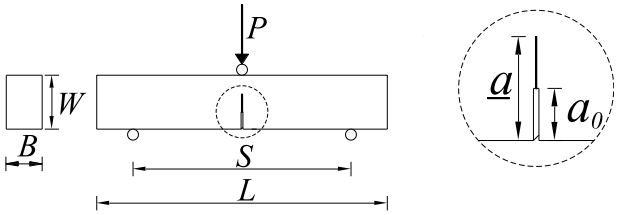

Fig. A.2. Geometrical and testing configuration of specimen according to the Two-Parameter Model.

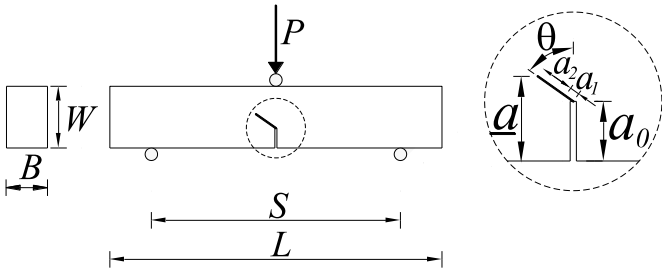

Fig. A.3. Geometrical and testing configuration of specimen according to the Modified Two-Parameter Model.

B. Micromechanical numerical model formulation

B.1. Homogenization technique

A fundamental hypothesis is the assumption that each fiber phase is homogeneously distributed inside the matrix and that a reference elementary volume (R.E.V.), having a characteristic length d, has the same average composition - and consequently the same mechanical properties – of the whole composite (Fig. B.1).

Moreover, the characteristic length D of the body is assumed to be greater than the characteristic length d of the R.E.V., i.e. $D/d >> 1$, and this implies that the composite is macroscopically homogeneous. Under such a hypothesis, very common in the modelling of the mechanical behavior of finite random heterogeneous bodies, the average properties of the composite material can be determined. This goal can be obtained by equating the virtual work rate evaluated in the composite material, with that related to a homogenized equivalent material [41], that is:

$$\int_V \dot{\tilde{\varepsilon}}(\mathbf{x}) : \left[k(\mathbf{x})\mathbf{C}_m(\mathbf{x}) + \sum_{p=1}^{q} X_p(x)\mathbf{C}_f^p(\mathbf{x}) \right] : \varepsilon(\mathbf{x}) dV = \int_V \dot{\tilde{\varepsilon}}(\mathbf{x}) : \mathbf{C}_{eq}(\mathbf{x}) : \varepsilon(\mathbf{x}) dV \tag{B.1}$$

where $\dot{\tilde{\varepsilon}}(\mathbf{x})$ and $\varepsilon(\mathbf{x})$ are the virtual strain rate tensor and the strain tensor, respectively, and $\mathbf{x}$ is the position vector that identifies the location of the point inside the body having volume V. $\mathbf{C}_m(\mathbf{x})$, $\mathbf{C}_f^p(\mathbf{x})$ and $\mathbf{C}_{eq}(\mathbf{x})$ are the matrix, *p-th* fiber phase and equivalent elastic tensors, respectively, whereas $\kappa(\mathbf{x})$ and $\chi_p(\mathbf{x})$ are scalar functions, identifying the location of the point $\mathbf{x}$ in the matrix or in the reinforcing phase, respectively, defined as:

$$\kappa(\mathbf{x}) = \begin{cases} 1 & \text{if}(\mathbf{x}) \in V_m \\ 0 & \text{otherwise} \end{cases} \quad \text{and} \quad \chi_p(\mathbf{x}) = \begin{cases} 1 & \text{if}(\mathbf{x}) \in V_f^p \\ 0 & \text{otherwise} \end{cases} \tag{B.2}$$

being V_m matrix volume and V_f^p *p-th* fiber phase volume.

Since the equivalent material is assumed to be macroscopically homogeneous, the elastic equivalent tensor $\mathbf{C}_{eq}(\mathbf{x})$ can be considered constant with respect to the position vector $\mathbf{x}$ and its averaged value over the volume V can be written as:

$$\mathbf{C}_{eq} = \mu_m \cdot \mathbf{C}_m + \sum_{p=1}^{n} \mu_f^p \cdot \mathbf{C}_f^p \tag{B.3}$$

where the matrix and *p-th* fiber phase volume fractions, μ_m and μ_f^p, respectively, are introduced.

In order to take into account the fiber orientation, two Gaussian-like probability density functions, $p_\phi(\phi)$ and $p_\vartheta(\vartheta)$, are used to identify the fiber axial direction through the two angles ϕ and ϑ (Fig. B.1). Consequently, the *p-th* fiber phase elastic tensors, $\mathbf{C}_f^p(\mathbf{x})$, may be written as [39]:

$$\mathbf{C}_f^p = E_f^p \int_0^\pi \int_0^\pi p_\phi(\phi) p_\vartheta(\vartheta) \cdot (\mathbf{F} \otimes \mathbf{F}) d\phi d\vartheta \tag{B.4}$$

being $(\mathbf{F}\otimes\mathbf{F})$ a fourth-order tensor with $\mathbf{F} = (\mathbf{k}\otimes\mathbf{k})$ ($\mathbf{k}$ is the unit vector identifying the direction of a single fiber).

All the above relationships have been obtained under the hypothesis of perfect bond at fiber-matrix interface.

B.2. Fiber-matrix debonding

As mentioned in Section 3.2, when an imperfect bond between the reinforcing fiber and the matrix takes place, a strain jump $\varepsilon_{m-f}(\mathbf{x})$ can be assumed to exist at the fiber-matrix interface. To quantify the "degree of sliding" between the fiber and the matrix, a function $s(\varepsilon_m^f(\mathbf{x}))$ is used. Such a function depends on the amount of the matrix strain evaluated in the fiber direction, $\varepsilon_m^f(\mathbf{x})$. A very simple and reasonable relationship for $s(\varepsilon_m^f(\mathbf{x}))$ can be assumed to be, as in the present case, the piecewise linear dependence shown in Fig. B.2. Such a relationship requires the inclusion of two characteristic strains, that is, $\overline{\varepsilon_{m1}^f}$ and $\overline{\varepsilon_{m2}^f}$, defining the matrix strain values at which debonding takes place and debonding is complete, respectively.

Since the fibers are short, it is more convenient to introduce an averaged scalar sliding function, $s(\overline{\varepsilon_m^f})$, of the sliding function $s(\varepsilon_m^f(\mathbf{x}))$ along the fiber axis.

The actual fiber-detachment is then taken into account in the *p-th* fiber phase elastic tensors, $\mathbf{C}_f^p(\mathbf{x})$, by properly reducing the fiber matrix elastic modulus according to the sliding function $E_f^p(s(\overline{\varepsilon_m^f}))$ as here reported [41]:

$$\mathbf{C}_f^p = E_f^p\left(s\left(\overline{\varepsilon_m^f}\right)\right) \int_0^\pi \int_0^\pi p_\phi(\phi) p_\vartheta(\vartheta) \cdot (\mathbf{F} \otimes \mathbf{F}) d\phi d\vartheta \tag{B.5}$$

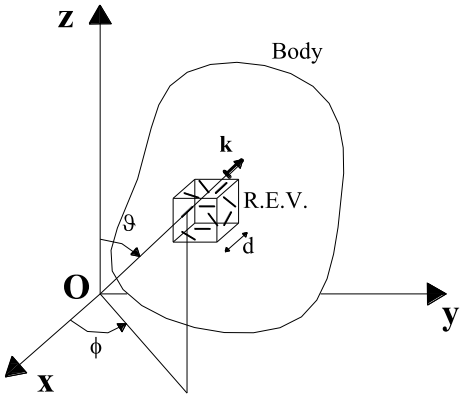

Fig. B.1. Body made of a fiber-reinforced composite material.

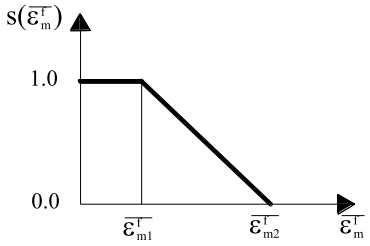

Fig. B.2. Simplified relationship for the sliding function at the fiber-matrix interface.

References

[1] ACI Committee 116R-00, Report on "Cement and Concrete Terminology". Report 116R-00, American Concrete Institute, Farmington Hills, Mich., 2000.

[2] ACI Committee 207.5R-99, Report on "Roller–Compacted Mass Concrete" Report 207R-99 (1999).

[3] Gentile G. Study, Preparation, and placement of low cement concrete, with special regard to its use in solid gravity dams, in: Transactions, International Congress on Large Dams, R16 Q 30. International Commission on Large Dams (ICOLD), Paris, France, 1964.

[4] ACI Committee 325.10R-95, Report on Roller-Compacted Concrete Pavements. 325.10R-95, American Concrete Institute, Farmington Hills, Mich., 1995.

[5] RW. Piggott, Roller Compacted Concrete Pavements: a Study of Long Term Performance. PCA R&D Serial No. 2261, Portland Cement Association, Skokie, Ill, 1999.

[6] A Gharibdoust, A Aldemir, B. Binici, Seismic behavior of roller compacted concrete dams under different base treatments, Struct. Infrastruct. Eng. 16 (2) (2020) 355–366.

[7] V Tang, T Nguyen, BB Igorevich, N Pham, T. Huynh, A combined experiment-simulation on temperature regime of roller-compacted concrete applying for dam construction, Int. J. Therm. Eng. 6 (2020) 772–785.

[8] A Aghaeipour, M. Madhkhan, Mechanical properties and durability of roller compacted concrete pavement (RCCP)—a review, Road Mater. Pavement Des. 21 (7) (2020) 1775–1798.

[9] S Debbarma, RN. Ransinchung, Achieving sustainability in roller compacted cocrete pavement mixes using reclaimed asphalt pavement aggregates—state of the art review, J. Clean. Prod. 287 (2021), 125078.

[10] PK Kolase, AK. Desai, Experimental study on monotonic and fatigue behavior of polypropylene fiber-reinforced roller-compacted concrete with fly ash, Road Mater. Pavement Des. 20 (5) (2019) 1096–1113.

[11] HE Fardin, A. Goulart dos Santos, Predicted responses of fatigue cracking and rutting on roller compacted concrete base composite pavements, Constr. Build. Mater. 272 (2021), 121847.

[12] E Rahmani, MK Sharbatdar, MHA. Beygi, A comprehensive investigation into the effect of water to cement ratios and cement contents on the physical and mechanical properties of roller compacted concrete pavement (RCCP), Constr. Build. Mater. 253 (2020), 119177.

[13] I Boussetta, S El Euch Khay, J. Neji, Experimental testing and modelling of roller compacted concrete incorporating RAP waste as aggregates, Eur. J. Environ. Civ. Eng. 24 (11) (2020) 1729–1743.

[14] I Aghayan, R Khafajeh, M. Shamsaei, Life cycle assessment, mechanical properties, and durability of roller compacted concrete pavement containing recycled waste materials, Int. J. Pavement Res. Technol. 14 (2021) 595–606.

[15] D Tavakoli, RS Dehkordi, H Divandari, J. de Brito, Properties of roller-compacted concrete pavement containing waste aggregates and nano SiO_2, Constr. Build. Mater. 249 (2020), 118747.

[16] SA Yildizel, G Calis, BA. Tayeh, Mechanical and durability properties of ground calcium carbonate-added roller-compacted concrete for pavement, J. Mater. Res. Technol. 9 (6) (2020) 13341–13351.

[17] SS Rahaman, MJ. Khattak, Roller compacted geopolymer concrete recycled concrete aggregate, Constr. Build. Mater. 283 (2021), 1322624.

[18] KH Raja, S Sajja, KS. Prakash, Experimental investigation of roller compacted concrete with industrial wastes, Int. J. Recent Technol. 7 (6) (2019) 585–588.

[19] H Suiffi, A El Maliki, F Majid, O. Cherkaoui, The effect of using polypropylene fibers on the durability and fire resistance of concrete, Frat. Integrita Strutt. 15 (58) (2021) 296–307.

[20] R Elsadany, SH Al-Tersawy, HEDM. Sallam, Effect of reinforcement type on structural behavior of RC beams containing recycled aggregate, Frat. Integrita Strutt. 16 (61) (2022) 294–307.

[21] T Messas, D Achoura, B Abdelaziz, B. Mamen, Experimental investigation on the mechanical behavior of concrete reinforced with Alfa plant fibers, Frat. Integrita Strutt. 16 (60) (2022) 102–113.

[22] YD Jia, ZW Zhou, YD Qu, AS. Tian, Experimental research on the fracture properties of roller compacted steel fiber recycled concrete, Adv. Mater. Res. 299–300 (2011) 135–138.

[23] JN Karadelis, Y. Lin, Flexural strengths and fiber efficiency of steel-fiber-reinforced, roller-compacted, polymer modified concrete, Constr. Build. Mater. 93 (2015) 498–505.

[24] J LaHucik, S Dahal, J Roesler, AN. Amirkhanian, Mechanical properties of roller-compacted concrete with macro-fibers, Constr. Build. Mater. 135 (2017) 440–446.

[25] M Haghnejad, A. Modarres, Effect of freeze-thaw cycles on the response of roller compacted concrete pavement reinforced by recycled polypropylene fiber under monotonic and cyclic loadings, Road Mater. Pavement Des. 22 (12) (2021) 2704–2720, https://doi.org/10.1080/14680629.2020.1794942.

[26] SB Singh, H Chawla, B. Ranjitha, Hybrid effect of functionally graded hybrid composites of glass-carbon fibers, Mech. Adv. Mater. Struct. 26 (14) (2019) 1195–1208.

[27] GT Truong, KK. Choi, Tensile behavior of hybrid composites of carbon fibers-steel wire mesh reinforced polymer, Mech. Adv. Mater. Struct. 28 (2) (2021) 154–166.

[28] S Guler, D Yavuz, Post-cracking behavior of hybrid fiber-reinforced concrete-filled steel tube beams, Constr. Build. Mater. 205 (2019) 285–305.

[29] AS Moghadam, F. Omidinasab, Assessment of hybrid FRSC cementitious composite with emphasis on flexural performance of functionally graded slabs, Constr. Build. Mater. 250 (2020), 118904.

[30] N Banthia, R. Gupta, Hybrid fiber reinforced concrete (HyFRC): fiber synergy in high strength matrices, Mater. Struct. 37 (2004) 707–716.

[31] D Scorza, R Luciano, S Mousa, S. Vantadori, Fracture behavior of hybrid fiber-reinforced roller-compacted concrete used in pavements, Constr. Build. Mater. 271 (2021), 121554.

[32] YS Jenq, SP. Shah, Two-Parameter fracture model for concrete, J. Eng. Mech. 111 (1985) 1227–1241.

[33] A Carpinteri, F Berto, G Fortese, C Ronchei, D Scorza, S. Vantadori, Modified two-parameter fracture model for bone, Eng. Fract. Mech. 174 (2017) 44–53.
[34] S Vantadori, A Carpinteri, G Fortese, C Ronchei, D. Scorza, Mode I fracture toughness of fiber-reinforced concrete by means of a modified version of the Two-Parameter Model, Proc. Struct. Integr. 2 (2016) 2889–2895.
[35] A Carpinteri, G Fortese, C Ronchei, D Scorza, S. Vantadori, Mode I fracture toughness of fiber reinforced concrete, Theor. Appl. Fract. Mech. 91 (2017) 66–75.
[36] O Benaimeche, A Carpinteri, M Mellas, C Ronchei, D Scorza, S. Vantadori, The influence of date palm mesh fiber reinforcement on flexural and fracture behavior of a cement-based mortar, Compos. B 152 (2018) 292–299.
[37] D Scorza, L Marsavina, A Carpinteri, C Ronchei, S. Vantadori, Size-effect independence of particleboard fracture toughness, Compos. Struct. 229 (2019) art. no111374.
[38] R Brighenti, D. Scorza, Numerical modelling of the fracture behavior of brittle materials reinforced with unidirectional or randomly distributed fibers, Mech. Mater. 52 (2012) 12–27.
[39] R Brighenti, D. Scorza, A micro-mechanical model for statistically unidirectional and randomly distributed fiber-reinforced solids, Math. Mech. Solids 17 (8) (2012) 876–893.
[40] R Brighenti, A Carpinteri, D. Scorza, Fracture mechanics approach for a partially debonded cylindrical fiber, Compos. B 53 (2013) 169–178.
[41] D Scorza. Mechanical Modelling of Short-Fibre-Reinforced Materials under Static or Cyclic Loading, ESIS Publishing House, 2021.
[42] R Brighenti, A Carpinteri, D. Scorza, Micromechanical crack growth-based fatigue damage in fibrous composites, Int. J. Fatigue 82 (2016) 98–109.
[43] RILEM Technical Committee, 50-FMC, Determination of the fracture energy of mortar and concrete by means of three-point bend test on notched beams, proposed RILEM draft recommendations, Mater. Struct. 18 (1985) 285–290.
[44] RILEM Technical Committee, 89-FMT, Determination of fracture parameters (KsIC and CTODc) of plain concrete using three-point bend tests, proposed RILEM draft recommendations, Mater. Struct. 23 (1990) 457–460.
[45] ASTM C 1176/C1176M, Standard Practice for Making Roller-Compacted Concrete in Cylinder Molds Using a Vibrating Table, American Society for Testing and Materials, 2013.
[46] AL Kalamkarov, HQ. Liu, A new model for a multiphase fiber-matrix composite materials, J. Solids Struct. 29 (1998) 643–653.
[47] HL. Cox, The elasticity and strength of paper and other fibrous materials, Br. J. Appl. Phys. 3 (1952) 73–79.
[48] R Brighenti, A Carpinteri, D. Scorza, Mechanics of interface debonding in fiber-reinforced materials, J. Compos. Mater. 50 (19) (2016) 2699–2718.
[49] JM Sancho, J Planas, DA Cendón, E Reyes, JC. Gálvez, An embedded crack model for finite element analysis of concrete fracture, Eng. Fract. Mech. 74 (2007) 75–86.